

AKARI NEAR-INFRARED SPECTROSCOPY OF THE EXTENDED GREEN OBJECT G318.05+0.09:
DETECTION OF CO FUNDAMENTAL RO-VIBRATIONAL EMISSIONTAKASHI ONAKA, TAMAMI MORI, ITSUKI SAKON AND ALEKSANDRA ARDASEVA¹

Department of Astronomy, Graduate School of Science, The University of Tokyo, 113-0033 Tokyo, Japan

¹School of Physics and Astronomy, University of St. Andrews, North Haugh, St Andrews, Fife, KY16 9SS, UK

ABSTRACT

We present the results of near-infrared (2.5–5.4 μm) long-slit spectroscopy of the extended green object (EGO) G318.05+0.09 with *AKARI*. Two distinct sources are found in the slit. The brighter source has strong red continuum emission with H₂O ice, CO₂ ice, and CO gas and ice absorption features at 3.0, 4.25 μm , 4.67 μm , respectively, while the other greenish object shows peculiar emission that has double peaks at around 4.5 and 4.7 μm . The former source is located close to the ultra compact H II region IRAS 14498–5856 and is identified as an embedded massive young stellar object (YSO). The spectrum of the latter source can be interpreted by blue-shifted ($-3000 \sim -6000 \text{ km s}^{-1}$) optically thin emission of the fundamental ro-vibrational transitions ($v = 1 - 0$) of CO molecules with temperatures of 12000–3700 K without noticeable H₂ and H I emission. We discuss the nature of this source in terms of outflow associated with the young stellar object and supernova ejecta associated with a supernova remnant.

Keywords: infrared: ISM — ISM: lines and bands — ISM: jets and outflows — ISM: supernova remnants — dust, extinction

1. INTRODUCTION

The *Spitzer* Galactic Legacy Infrared Mid-Plane Survey Extraordinaire (GLIMPSE; Benjamin et al. 2003) has discovered a new class of interesting objects that show extended bright emission at the IRAC band 2 (4.5 μm), called Extended Green Objects (EGOs, Cyganowski et al. 2008). EGOs are often discussed in terms of candidates of massive young stellar objects (YSOs) with outflows. The greenish color is attributed either to H₂ ($v = 0 - 0$, S(9, 10, 11)) lines and CO ($v = 1 - 0$) band heads excited by shocks, or scattered light in the outflow cavity (e.g., Noriega-Crespo et al. 2004; Smith et al. 2006; Cyganowski et al. 2008; Qiu et al. 2008; Tobin et al. 2008). Takami et al. (2010, 2012) make detailed analysis of the origin of the excess emission based on photometric data of EGOs and conclude that extra components other than H₂ emission are needed to explain the excess emission at 4.5 μm and that continuum emission of the scattered light in the outflow cavity is likely the primary origin of the excess, which is supported by Lee et al. (2013). Supernova remnants (SNRs) also show excess emission at 4.5 μm due to H₂ and CO molecular bands (Reach et al. 2006). While H₂

emission is thought to dominate in the line emission, the contribution from CO emission becomes comparable to that from H₂ for the H₂ density of a range $10^6 - 10^7 \text{ cm}^{-3}$ (Neufeld & Yuan 2008). CO ($v = 1 - 0$) emission is not detected in the SNR IC443 by ground-based observations (Richter et al. 1995), but it is detected toward the Orion molecular cloud (OMC Geballe & Garden 1987, 1990; González-Alfonso et al. 2002), suggesting that CO emission could make a contribution to the excess emission.

It is indispensable to make spectroscopic observations in order to study the origin of the excess at 4.5 μm in EGOs unambiguously. However, no direct spectroscopy has so far been made for EGOs except for the 2 μm region (Caratti o Garatti et al. 2015) due to the lack of sensitive spectrometer in the 4 μm region. In *this paper*, we report the result of spectroscopy in 2.0–5.3 μm of one of the EGOs, G318.05+0.09, made with the Infrared Camera (IRC) onboard *AKARI*, which offered high-sensitivity spectroscopy in 2.0–5.3 μm even in its warm mission phase (Onaka et al. 2010).

2. OBSERVATIONS AND DATA REDUCTION

The *AKARI* /IRC observation of G318.05+0.09 was carried out in the director time on 2010 February 18, which was one of the last observations of the *AKARI* mission (Observation I.D.: 5201570.1). The observa-

tion was made with the slit spectroscopy mode at the Ns slit of $5''$ width with the prism and grism dispersers (AOT IRCZ4 with c;Ns). The prism spectroscopy provides spectra of $2.0\text{--}5.3\mu\text{m}$ with the spectral resolution of about $0.14\mu\text{m}$ at $4\mu\text{m}$, while spectra of $2.5\text{--}5.0\mu\text{m}$ with the resolution of about $0.03\mu\text{m}$ are obtained with the grism. In the present observation, four exposure frames with the prism were first taken and then five exposures with grism were performed, which sandwiched a $3.2\mu\text{m}$ -band imaging observation in-between that was used for the position determination (see Onaka et al. 2007; Ohyama et al. 2007, for more details of the IRC spectroscopy). It provided long slit spectroscopy of about $40''$ long along the slit direction. The slit location is shown in Figure 1 superimposed on the *Spitzer*/IRAC artificial three-color image together with the positions of the known sources in the catalogs (see Table 1). The slit of the present observation runs from an infrared bright region at the western edge, which is most likely to be IRAS 14498–5856, although the catalog position is slightly different from the bright source (cross #3 in Fig. 1). The slit covers a greenish blob at around its center. The two distinct sources are clearly seen in the long-slit spectrum image. We call the bright source *S1* and the greenish blob *S2* in the following. Spectra are extracted from $5'' \times 8.7''$ (6 pixels in the slit direction) areas indicated by the yellow and white boxes both for the grism and prism data. The former corresponds to *S1* and the latter to *S2*. The slit area of *S1* does not collect the entire emission from the bright source. EGO G318.05+0.09 is defined by a diamond-like shape area of $\sim 35'' \times 10''$, whose center is located at slightly north of the bright source as marked by cross #2. It extends to the east and west directions symmetrically to enclose the bright source and cover the greenish regions, including *S2* (Fig. 3.14 of Cyganowski et al. 2008). The present *AKARI*/IRC spectroscopy covers only the eastern part of G318.05+0.09. The center position of EGO G318.05+0.09 is located in the region for which the spectrum of *S1* is extracted. The methanol maser source MMB 318.050+0.087 (Caswell 2009; Green et al. 2012) is also located within the box of *S1* (cross #1). Table 1 summarizes the central positions of the regions where the spectra are extracted together with the known sources in this region.

The data reduction was performed with the latest toolkit for the phase 3 (warm mission phase) of the IRC spectroscopy, IRC_SPEC_TOOLKIT.P3_20150331¹. Since the observation was made in the very last period of the warm mission phase of *AKARI*, the effect of

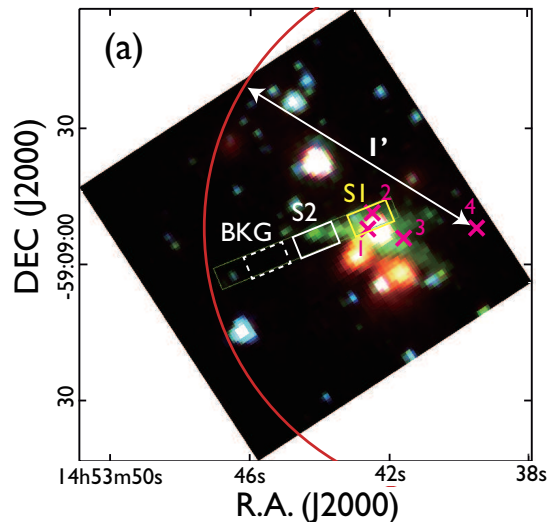


Figure 1. *Spitzer*/IRAC artificial three-color image of the region of EGO G318.05+0.09 and the slit position of the present *AKARI*/IRC spectroscopy (blue: IRAC band 1 ($3.6\mu\text{m}$), green: IRAC band 2 ($4.5\mu\text{m}$) and red: IRAC band 3 ($5.8\mu\text{m}$)). The thin green rectangle indicates the location of the IRC Ns slit ($5'' \times 40''$). The western yellow box, the center white box, and the eastern white dotted box in the slit indicate the regions for which the spectra of *S1*, *S2* and the background emission are extracted, respectively. The yellow box for which the spectrum of *S1* is extracted includes part of the bright source. The crosses indicate the positions of the known sources in the catalogs (Table 1). The sources are labeled by the numbers: 1 is the methanol maser source (Caswell 2009; Green et al. 2012), 2 EGO G319.05+0.09 (Cyganowski et al. 2008), 3 IRAS 14498–5856, and 4 Source B of *BeppoSAX* observations (Bocchino et al. 2001). The red circle shows its error circle of the X-ray source position (*I'*). The IRAC data are retrieved from the NASA/IPAC Infrared Science Archive.

hot pixels became severe and the noise level was higher than typical values in the phase 3 spectroscopy (Onaka et al. 2010). To remove residual dark current and possible contribution from the surrounding background/foreground emission, we subtract the emission enclosed by the white rectangle in the eastern part of the slit labeled by BKG in Figure 1. There is a shift in the slit position on the detector array between the grism and prism spectroscopy due to the optical alignment. The amount of the shift is estimated by matching the bright region and the spectra of the same region are extracted within an accuracy of a half pixel ($\sim 0.8''$) along the slit direction for the grism and prism modes. Details of the data reduction are summarized in Mori et al. (2014). Due to the relatively large number of hot pixels, a few residual hot pixels remain after the standard reduction process. They are masked manually. The masked pixels are at $4.457\mu\text{m}$ and $4.5154\mu\text{m}$ of the grism spectrum of *S1* and at $3.9607\text{--}3.9801\mu\text{m}$ in the grism spectrum of *S2* and they do not affect the following discussion. It should also be

¹ <http://www.ir.isas.jaxa.jp/AKARI/Observation/support/IRC/>

noted that the absolute calibration may have a large uncertainty ($\sim 20\%$) due to the elevated temperature of the detector array at the observing time (~ 47.5 K) because the sensitivity is not well calibrated at warm temperatures, while no change in the spectral response due to the change in the temperature is recognized (Onaka et al. 2010). We have not applied correction for the contamination of the second order light for the grism spectra in the phase 2 (cold mission phase)

recently reported by Baba et al. (2016) because there is no calibration of the contamination estimate available for the phase 3 data at present. Instead we discard the data in the spectral region where the contamination is expected ($> 4.9 \mu\text{m}$). The improved wavelength calibration provided by Baba et al. (2016) is applied to the present grism spectra. The correction for wavelengths longer than $4 \mu\text{m}$ is not significant ($< 0.006 \mu\text{m}$) compared to the instrumental spectral resolution.

Table 1. Positions of the sources in the G318.05+0.09 region

Source name	R.A. (J2000)	Decl. (J2000)	Note	Number in Fig. 1
S1	14 53 42.2	-59 08 48.8	Present work ^a	
S2	14 53 44.0	-59 08 54.3	Present work ^a	
MMB318.050+0.087	14 53 42.67	-50 08 52.4	Methanol maser ^b	1
G318.05+0.09	14 53 42.6	-59 08 49	EGO ($\sim 35'' \times 10''$) ^c	2
IRAS 14498-5856	14 53 41.6	-59 08 54	UCH II ^d	3
Source B	14 53 39.5	-59 08 52	X-ray source ^e	4
G318.2+0.1	14 54 50	-59 46	SNR ^f	outside of Fig. 1

^aThe center position from which the spectrum is extracted in the slit.

^bCaswell (2009); Green et al. (2012)

^cCyganowski et al. (2008)

^dWalsh et al. (1997)

^eBocchino et al. (2001)

^fWhiteoak & Green (1996)

3. RESULTS

Figure 2 shows the extracted spectra of S1 and S2. There is apparent discrepancy between the grism and prism spectra of S1 in $4\text{--}5 \mu\text{m}$. We attribute the difference to the saturation effect of the prism spectrum since S1 is very bright for the prism spectroscopy in phase 3. The grism spectrum does not have a saturation problem at this brightness level and thus we regard it more reliable. The grism spectrum shows absorption features at around 3.0 , 4.25 , and $4.67 \mu\text{m}$ clearly, whose traces are also seen in the prism spectrum. The former two can be attributed to H₂O and CO₂ ice absorption, and the latter to CO gas or ice absorption. To estimate the absorption features quantitatively, we fit the continuum by a spline curve with anchor points at 2.6 , 2.65 , 3.8 , 4.1 , 4.4 , and $4.9 \mu\text{m}$ (thin brown dotted line in Fig. 2).

For the H₂O ice absorption profile, the laboratory data taken at 10 K are adopted (Ehrenfreund et al. 1996). We find that an extra “red wing” component is needed to fit the $3 \mu\text{m}$ absorption feature in addition to the

laboratory data profile. The red wing is seen in many objects, but its origin is not yet fully understood (e.g., Smith et al. 1993; Thi et al. 2006; Noble et al. 2013). In the present fit, it is approximated by a Gaussian profile with the central wavelength of $3.35 \mu\text{m}$ and the FWHM of $0.31 \mu\text{m}$. Figure 3a shows details of the fit of the $3 \mu\text{m}$ absorption feature in units of the optical depth.

We assume a Gaussian function for the CO₂ ice feature at $4.25 \mu\text{m}$ because it is narrow compared to the present spectral resolution and use the band strengths of CO₂ in Gerakines et al. (1995) to estimate the column density. The observed profile is well fitted by a Gaussian with the central wavelength of $4.25 \mu\text{m}$ and the FWHM of $0.036 \mu\text{m}$. The FWHM is adopted from the study of AKARI/IRC Ns spectroscopy of Galactic star-forming regions (Mori et al. 2014). The central wavelength of the absorption peak of CO₂ ice is slightly shorter than the typical value of $4.26 \mu\text{m}$ obtained in the same study, but it is still within the uncertainty due to the large noise level and the spectral resolution of the present observation. The absorption

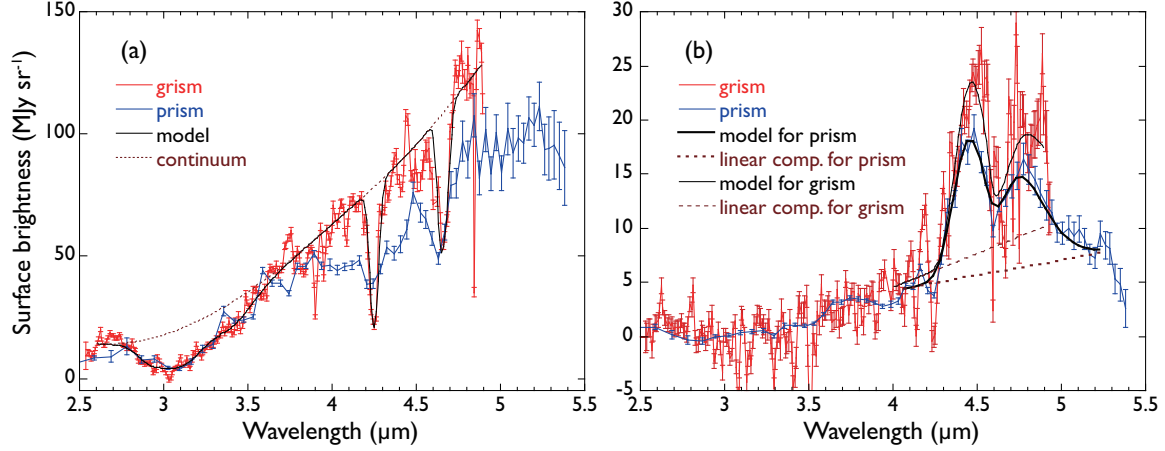


Figure 2. *AKARI*/IRC near-infrared spectra of (a) *S1* and (b) *S2*. The red lines indicate spectra taken with grism, while the blue lines show those with prism. In (a) the model spectrum with ice and gas absorption features and the assumed continuum are shown by the solid black and dotted brown lines, respectively, for the grism spectrum. In (b) the model spectra with CO emission with linearly increasing components are shown by the thick and thin black lines for the prism and grism spectra, respectively. The assumed linear component is shown by the thick and thin brown dotted lines for the prism and grism spectra, respectively. For the prism spectrum, the CO emission is assumed to have the temperature of 1600 K and the velocity of -4700 km s^{-1} , while they are assumed to be 2000 K and -4100 km s^{-1} for the grism spectrum (see text for details).

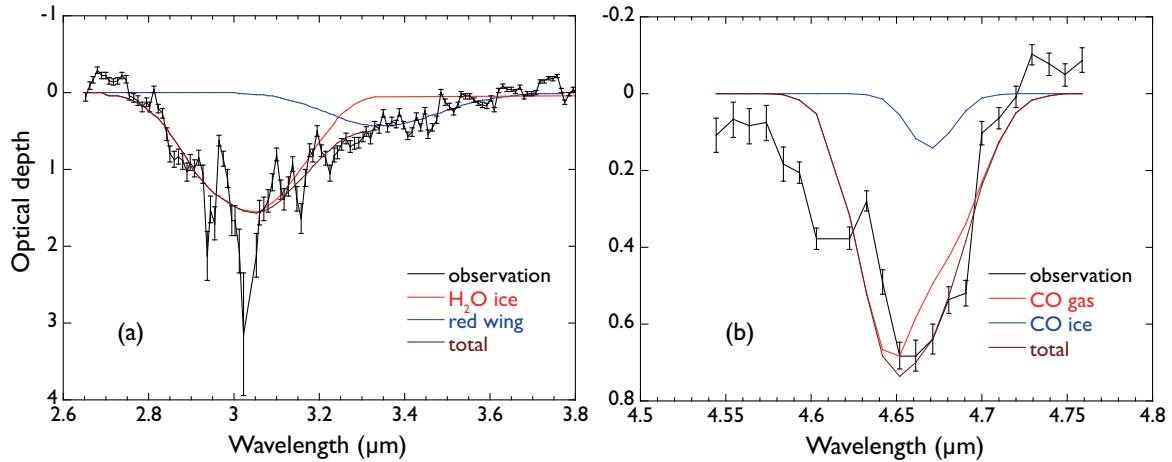


Figure 3. Absorption features and model fits in units of the optical depth for the grism spectrum of *S1*. (a) $3 \mu\text{m}$ region and (b) $4.67 \mu\text{m}$ region. (a) The black line shows the observation, the red line the H_2O ice component, the blue line the red wing component approximated by a Gaussian function, and the brown line the summation of H_2O ice and the red wing. (b) The black line shows the observation, the red line the CO gas component of 20K, the blue line the CO ice component approximated by a Gaussian, and the brown line the summation of the CO gas and ice features.

feature at around $4.67 \mu\text{m}$ is broader than the CO ice feature (Gibb et al. 2004; Mori et al. 2014). We fit it with both CO gas and ice components. For CO ice, we adopt the central wavelength of $4.67 \mu\text{m}$ and the FWHM of $0.031 \mu\text{m}$ obtained from the Ns spectroscopy by Mori et al. (2014) and assume the band strength reported in Gerakines et al. (1995). The observed feature can be fitted by absorption of CO gas at 20K and CO ice as shown in Fig. 3b. The contribution from CO gas dominates in the absorption. With the present spectral resolution, the P and R branches of CO gas absorption are not resolved. The red side is relatively well fitted, while the fit is not good at the blue side, where there might be an additional component at around $4.62 \mu\text{m}$.

Because of the large noise, however, it is difficult to make further discussion on the additional component. CO gas with 15–30 K gives similar fits and the gas temperature cannot be well constrained. As Fig. 3 suggests, the contribution from CO ice also has a large uncertainty. Therefore, the present estimate of the column densities of CO gas and ice should be taken with caution. The derived column densities are (26.3 ± 0.5) , (3.42 ± 0.03) , (2.0 ± 0.5) , and $(62 \pm 2) \times 10^{17} \text{ cm}^{-2}$ for H_2O ice, CO_2 ice, CO ice, and CO gas, respectively.

Source *S2* shows a peculiar spectrum. It does not show emission features at $3.3\text{--}3.5 \mu\text{m}$, which are generally seen in star-forming regions and are attributed to polycyclic aromatic hydrocarbons (Mori et al. 2014),

nor ice absorption features seen in YSOs as in *S1*. It shows two broad peaks at around 4.5 and $4.7\ \mu\text{m}$ and no significant emission is seen below $4\ \mu\text{m}$. Both the prism and grism spectra show similar characteristics and thus we conclude that these are real features despite the noisy spectra. A small difference between the grism and prism spectra is seen at wavelengths longer than $4.5\ \mu\text{m}$. It can be attributed partly to the large noise in the grism spectrum and/or to a possible difference in the spectrum extracted region due to the shift of the slit positions on the detector array (see §2).

The *S2* spectrum can be accounted for by blue-shifted optically thin emission of the fundamental ro-vibrational transitions ($v = 1 - 0$) of CO molecules with red continuum. The two peaks are attributed to the P and R branches of CO gas emission. Since the grism spectrum is very noisy and does not have data longer than $4.9\ \mu\text{m}$, we use the prism spectrum to estimate the temperature and the velocity of the CO gas. We simply assume that the continuum increases linearly with the wavelength and the CO emission is approximated by the local thermodynamic equilibrium (LTE) condition. From the fit, the temperature and the velocity of the CO gas are estimated as $1600^{+500}_{-400}\ \text{K}$ and $-4700^{+1200}_{-1500}\ \text{km s}^{-1}$, respectively. The grism spectrum requires more steeply increasing continuum, but the best fit parameters of the CO gas ($2000\ \text{K}$ and $-4100\ \text{km s}^{-1}$) are within the uncertainties estimated from the prism spectrum. The model spectra with the best fit parameters are shown in Fig. 2b both for the prism (thick black line) and grism spectra (thin black line) together with the linear continuum (thick and thin dotted brown lines). The column density of the CO gas is estimated from the prism spectrum with the best fit parameters as $(1.2 \pm 0.1) \times 10^{10}\ \text{cm}^{-2}$, which does not include the systematic error due to the calibration uncertainty at the time of the observation (§2).

The shift in the wavelength corresponding to the estimated blue-shift velocity is $-0.06 \sim -0.07\ \mu\text{m}$, which is about a half of the resolution of the prism spectrum, but more than twice of that of the grism spectrum at $4.5\ \mu\text{m}$. The latest wavelength calibration of the grism spectroscopy has been applied (§2, Baba et al. 2016) and the accuracy is estimated to be better than $0.006\ \mu\text{m}$, which is much smaller than the shift. The wavelength calibration of the prism spectroscopy is less accurate and estimated to be better than 1 pixel or $0.04\ \mu\text{m}$ at $4\text{--}5\ \mu\text{m}$ (Onaka et al. 2009). The comparison of the prism and grism spectroscopy confirms that both wavelengths match with each other within this accuracy (Mori et al. 2014).

The shift is constrained by the profile shape of the CO emission in the fit and non-LTE effects could affect the shift estimate. To investigate the reliability of

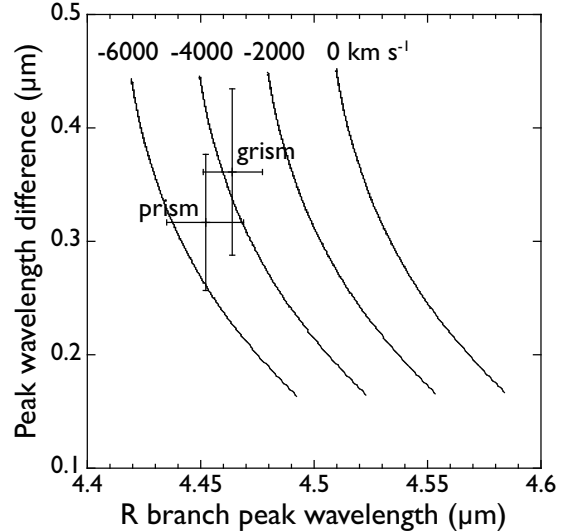


Figure 4. Difference in the peak wavelengths of the R and P branches of CO fundamental ro-vibrational emission are plotted against the peak wavelength of the R branch. Those from the observed *S2* spectra with the prism and grism are shown by the crosses with the error bars. The error bars include the uncertainties in the Gaussian fit and the effect of the underlying continuum slope. The former uncertainties dominate in the errors. The solid lines indicate the values estimated from the LTE CO emission for temperatures of $500\text{--}4000\ \text{K}$ with the different blue-shift velocities labeled at the top of the lines. The bottom of the lines corresponds to $T = 500\ \text{K}$ and the top to $T = 4000\ \text{K}$.

the suggested large blue-shift velocity, we simply calculate the peak positions of the observed spectra and compare them with those of the LTE model spectra of different temperatures. The peak positions are estimated by a Gaussian fit in the ranges $4.3\text{--}4.6\ \mu\text{m}$ and $4.65\text{--}4.9\ \mu\text{m}$ for the R and P branches, respectively. We also vary the slope of the underlying continuum for $2\text{--}7\ \text{MJy sr}^{-1}\ \mu\text{m}^{-1}$, which is determined by the range of the slopes obtained in the CO profile fit. The effect of the continuum slope is found to be smaller (< 0.005 and $< 0.01\ \mu\text{m}$ for the R and P branches, respectively) than the uncertainties in the Gaussian fits both for the prism and grism spectra. The peaks of the model CO emission are estimated in the same manner.

Figure 4 plots the difference between the P and R branch peak wavelengths against the estimated peak wavelength of the R branch both for the prism and grism spectra together with those of the model CO emission for the temperature range $500\text{--}4000\ \text{K}$ with the various blue-shift velocities. The peak wavelength is sensitive both to the temperature and the blue-shift velocity, but the difference in the branch peaks is sensitive mostly to the temperature. The latter is used to separate the temperature effect from the velocity effect. The peak wavelength of the R branch of the prism spectrum agrees with that of the grism spectrum within the calibration uncertainty of the prism spectroscopy. The prism and

grism spectra show compatible values for the difference in the R and P branch peak wavelengths within the uncertainties in the fit. Both data points suggest that the observed spectra can be accounted for by CO emission with blue-shift velocities of $-3000 \sim -6000 \text{ km s}^{-1}$ and that it is difficult to explain the observed peak wavelengths by simple LTE models with velocities larger than -2000 km s^{-1} . The suggested temperatures of the CO emission range from 1200 to 3700 K, which are in agreement with the CO emission profile fit. While these analyses suggest a large blue-shift velocity consistently, the present spectra do not have a high signal-to-noise ratio and good spectral resolution. Spectra with higher spectral resolution and better quality are needed to investigate the non-LTE effects and confirm the large blue-shift velocity.

4. DISCUSSION

4.1. Nature of *S1*

Source *S1* is located close to the position of IRAS 14498–5856. The IRAS source is classified as an ultra compact H II (UCH II) region based on the *IRAS* colors and methanol maser emission at 6668 MHz is detected toward this object (Walsh et al. 1997). The position of the maser is accurately measured by Caswell (2009), which matches well with the position of *S1* (Fig. 1 and Table 1). The methanol maser at 6668 MHz is known as a good tracer for the early stages of high-mass star formation (Green et al. 2012, and references therein). The center position of the EGO G318.05+0.059 is close to the maser position and it is suggested to be a likely massive YSO outflow candidate in the EGO catalog (Cyganowski et al. 2008). The *AKARI*/IRC spectrum of *S1* shows the absorption features of H₂O and CO₂ ices clearly. These ice absorption features are also characteristics of embedded YSOs (e.g., Gibb et al. 2004; Shimonishi et al. 2010). The column densities of CO₂ and H₂O ices are known to show a correlation in YSOs and the ratio depends on the nature of the object (Gerakines et al. 1999; Nummelin et al. 2001; Pontoppidan et al. 2008). The abundance ratio of CO₂ to H₂O ices in *S1* is $13.0 \pm 0.3\%$, being within the range of the ratios found for weakly processed ices in massive YSOs in our Galaxy (13–23%, Gibb et al. 2004). The CO ice absorption is generally not abundant. While the relative abundance of CO ice to CO₂ ice varies with the line of sight (Pontoppidan et al. 2008; Noble et al. 2013), the present relative abundance ($7.6 \pm 1.9\%$ relative to H₂O ice) is also within the range found for weakly processed ices in massive YSOs (3–8%, Gibb et al. 2004). All of these pieces of evidence suggest that *S1* is most likely an embedded massive YSO. Walsh et al. (1997) estimate a kinematic distance

to the maser source as 4.3 or 11.1 kpc from its velocity (-46 km s^{-1}). An X-ray source has also been detected by *BeppoSAX* in this region (Source B in Bocchino et al. 2001). Source *S1* is located within the error circle of the position of the X-ray source (#4 in Fig. 1). Bocchino et al. (2001) suggest that if the X-ray source is the hard X-ray counterpart of the UCH II, the shorter distance is favored since the X-ray luminosity becomes too high as an UCH II at 11.1 kpc.

The area from which the spectrum of *S1* is extracted includes greenish emission as Fig. 1 suggests and thus the spectrum may have a contribution from CO emission. The prism spectrum of *S1* suggests a peak at around $4.5 \mu\text{m}$. It may mimic the R branch of CO emission seen in the spectrum of *S2*. However, the prism spectrum does not show a P-branch peak at around $4.7 \mu\text{m}$ clearly as seen in *S2*. Therefore, we conclude that the peak at around $4.5 \mu\text{m}$ is a result of a combination of the saturation effect and the cold CO gas absorption and that there is no clear evidence for warm CO emission in the spectrum of *S1*.

4.2. Nature of *S2*

Source *S2* shows a quite distinct spectrum. It can be interpreted in terms of highly blue-shifted CO emission with red continuum. In the following, we discuss two possibilities for its nature: (1) outflow associated with the YSO and (2) supernova ejecta associated with a SNR.

Excess emission at $4.5 \mu\text{m}$ in EGOs has often been discussed in terms of outflows associated with massive YSOs. Since *S1* is most likely a massive YSO, *S2* could be related to outflow associated with *S1*. Observations with the Short-Wavelength Spectrometer (SWS) on board the Infrared Space Observatory (*ISO*) detect the fundamental ro-vibrational ($v = 1 - 0$) emission of CO molecules toward the OMC-1 outflow region together with emission of H I recombination lines and H₂ lines (Rosenthal et al. 2000). The SWS observations of OMC-1 resolve each transition of the CO emission and thus the physical conditions of the CO gas and excitation mechanism are investigated in detail (González-Alfonso et al. 2002). The observed spectra show stronger emission of the P branch than that of the R branch. González-Alfonso et al. (2002) conclude that the CO emission consists of warm ($T = 200 - 400 \text{ K}$) and hot ($T \sim 3000 \text{ K}$) components and the P-R-asymmetry can be accounted for by a large CO column density ($\sim 6 \times 10^{18} \text{ cm}^{-2}$). Detection of the CO ro-vibrational emission toward OMC-1 supports the possible association of *S2* with outflow from *S1*. However, the characteristics of OMC-1 CO emission are different from the spectra of *S2*. There seem to be no H I recombination lines and H₂ lines in the grism spectrum of *S2*, which

are seen in OMC-1. There is excess emission at around the position of 0-0 S(11) ($4.1810\ \mu\text{m}$) in the grism spectrum of *S2*, but the absence of similar excess emission at 0-0 S(9) ($4.6847\ \mu\text{m}$), 0-0 S(10) ($4.4096\ \mu\text{m}$), and 0-0 S(13) ($3.8464\ \mu\text{m}$) suggests that the excess at $\sim 4.2\ \mu\text{m}$ is not H_2 0-0 S(11) emission.

To discuss the implication of non-detection of H_2 line emission in *S2*, we make a simple comparison with the spectrum of OMC-1. The total CO $v = 1 - 0$ emission flux at Peak 1 of OMC-1 is estimated as $3.8 \times 10^{-13}\ \text{W m}^{-2}$ and that of the hot component is $1.7 \times 10^{-13}\ \text{W m}^{-2}$ (González-Alfonso et al. 2002). The fluxes of the four strongest lines of H_2 at Peak 1 in $3.5 - 5\ \mu\text{m}$, 0-0 S(9), 0-0 S(10), 0-0 S(11), and 0-0 S(13), are estimated as 3.2, 0.83, 1.4, and $0.92 \times 10^{-14}\ \text{W m}^{-2}$, respectively (Rosenthal et al. 2000). The total CO $v = 1 - 0$ emission intensity from *S2* is estimated as $1.75 \times 10^{-6}\ \text{W m}^{-2}\ \text{sr}^{-1}$. If the same ratios of the H_2 line intensities to the total CO emission as in OMC-1 are assumed, the expected H_2 line intensities in *S2* are 15, 3.8, 6.5, and $4.2 \times 10^{-8}\ \text{W m}^{-2}\ \text{sr}^{-1}$ for 0-0 S(9), 0-0 S(10), 0-0 S(11), and 0-0 S(13), respectively. If the H_2 emission is associated only with the hot CO component in OMC-1, the expected intensities are 34, 8.5, 14, and $9.4 \times 10^{-8}\ \text{W m}^{-2}\ \text{sr}^{-1}$ for 0-0 S(9), 0-0 S(10), 0-0 S(11), and 0-0 S(13), respectively. Three- σ upper limits of the line intensity in the *S2* grism spectrum are estimated as 1.8, 1.7, 4.5, and $1.6 \times 10^{-8}\ \text{W m}^{-2}\ \text{sr}^{-1}$, respectively, for 0-0 S(9), 0-0 S(10), 0-0 S(11), and 0-0 S(13). The upper limit on 0-0 S(11) is relatively large compared to the others due to the excess emission described above. All of these upper limits are smaller than the expected intensities estimated from the spectrum of Peak 1 of OMC-1. Thus, the H_2 line emission relative to the CO emission in *S2* are weak compared to that in OMC-1. González-Alfonso et al. (2002) show that a high H_2 density ($10^7\ \text{cm}^{-3}$) is required to account for the observed flux of the hot component of CO emission in OMC-1. They also find that the derived CO column density of the hot component ($\sim 1.8 \times 10^{17}\ \text{cm}^{-2}$) is much larger than that expected from the column density of hot H_2 component ($2.4 \times 10^{19}\ \text{cm}^{-2}$, Rosenthal et al. 2000), suggesting partial dissociation of H_2 in the region. Neufeld & Yuan (2008) also show that CO emission becomes comparable to H_2 emission in IRAC band 2 only at high gas densities ($10^6 - 10^7\ \text{cm}^{-3}$). Non-detection of H_2 line emission in *S2* may thus suggest even more H_2 -poor conditions than in OMC-1. A detailed study of the physical conditions of CO and H_2 in *S2* is definitely needed by observations with higher spectral resolution to make quantitative discussion. It should be noted that the suggested large blue-shift velocity, which also has to be confirmed by further observations, seems to be difficult to be explained if the CO emission of *S2* originates

from outflow associated with *S1*.

Spectra of *S2* show strong similarity to those detected toward ejecta knots in the SNR Cas A (Rho et al. 2012). The suggested blue-shift velocity of *S2* is in the range of those found in ejecta of Cas A ($-340 \sim -5660\ \text{km s}^{-1}$) and is attributed to the ejecta motion. The Cas A spectra do not show H I recombination lines and H_2 emission lines either, which can be attributed to hydrogen-poor abundance of the ejecta.

EGO G318.05+0.09 is located within the SNR G318.2+0.1, which is recognized by a large ($40' \times 35'$) radio shell (Whiteoak & Green 1996). However, there is no direct evidence that *S2* is associated with SN ejecta. No associated infrared emission has been found for this SNR region by the study of the GLIMPSE survey (Reach et al. 2006). The present EGO is a very tiny portion of the entire SNR G318.2+0.1 and this is very different from Cas A, in which extended infrared emission associated with SNR ejecta features is clearly detected. Toward the region of the SNR G318.2+0.1, only *BeppoSAX* observations are available in the X-ray (Bocchino et al. 2001), which have a large error circle (Fig. 1) and do not provide clear evidence for the association of *S2* with SN ejecta. While the characteristics of the spectra of *S2* suggest emission from SN ejecta, there is no other supporting evidence for the identification as ejecta at present.

If *S2* found in the present observation is truly SN ejecta, this will be the second SNR that shows CO emission at $4\ \mu\text{m}$. SNe are thought to be the major dust suppliers in the interstellar space as well as in the early Universe (Gall et al. 2011). However, mid-infrared observations of SNe so far suggest that the mass of the warm dust associated with SNe falls below $10^{-2}\ M_\odot$, significantly lower than theoretical predictions (Tinyanont et al. 2016, references therein). Recent far-infrared observations detect a significant amount ($>0.1\ M_\odot$) of cold dust associated with a SN or a SNR (Barlow et al. 2010; Sibthorpe et al. 2010; Matsuura et al. 2011; Gomez et al. 2012; Temim & Dwek 2013; Indebetouw et al. 2014; Lau et al. 2015; Matsuura et al. 2015). Detection of SNe and SNRs in the far-infrared is, however, limited to a small number of objects and the dust production yield in SNe still remains under debate (e.g., Gall et al. 2011). Recent observations also reveal the presence of several molecules in SNe or SNRs, such as SiO (Kotak et al. 2006), CO (Kamenetzky et al. 2013), and ArH^+ (Barlow et al. 2013). The presence of CO gas is of particular interest since CO traps the major dust-constituting element carbon and may reduce the carbon dust formation yield significantly (Clayton et al. 2001). CO molecules have been detected in about 10 SNe within 340 years after explosion. Cas A is a SNR of 340

years old and it is the only SNR in which both high-J rotational and ro-vibrational lines of warm CO gas have been detected (Rho et al. 2012; Wallström et al. 2013). Processing and evolution of dust and gas in SN ejecta after the explosion, in particular the effects of the reverse shock, have been becoming an important issue for the understanding of the net dust formation yield in SNe (Bianchi & Schneider 2007; Nozawa et al. 2007, 2010; Nath et al. 2008; Silvia et al. 2010, 2012; Gall et al. 2014; Dwek & Arendt 2015; Wesson et al. 2015; Biscaro & Cherchneff 2016). Biscaro & Cherchneff (2014) show that dust and molecules in ejecta clumps are destroyed by the reverse shock, whereas CO gas can reform in the post-reverse shock gas, but dust clusters do not. Processing of dust and gas in the post-reverse shock clumps depends sensitively on the environmental conditions (Biscaro & Cherchneff 2016). While no information is available of the SNR with which *S2* is associated, if it is confirmed to be SN ejecta, further studies of *S* will provide important information on the study of the physical and chemical conditions of the ejecta.

The presently available data for EGO G318.05+0.09 are not sufficient to draw a clear conclusion on the nature of *S2*. Spectroscopy with high spectral resolution and good quality are definitely needed to study the physical conditions of the CO gas and to confirm the large blue-shift velocity. Future observations with *JWST*/NIRSpec will certainly give us crucial information for the identification. X-ray observations with high spatial resolution and good energy resolution of *Chandra* will also help identify the nature of *S2*.

5. SUMMARY

We carried out near-infrared spectroscopy of the EGO G318.05+0.09 with *AKARI*/IRC. We have detected two distinct infrared sources in the region. One, *S1*, is associated with the UCH II IRAS 14498–5856 and identified as an embedded massive YSO based on the presence of the absorption features due to H₂O and CO₂ ice species together with the associated methanol maser emission. The other greenish-color source, *S2*, shows a quite peculiar spectrum, which has double peaks at around 4.5 and 4.7 μm . We attribute the emission to highly blue-shifted ($-3000 \sim -6000 \text{ km s}^{-1}$) fundamental ro-vibrational transitions ($v = 1-0$) of CO molecules of temperatures of 1200–3700 K with red continuum.

We discuss two possibilities of the nature of *S2*: out-

flow associated with *S1* and supernova ejecta. Detection of the CO fundamental ro-vibrational emission toward OMC-1 supports the association of *S2* with outflow from the massive YSO *S1*, although the characteristics of the CO emission are different. From simple comparison with the *ISO*/SWS spectra of OMC-1, non-detection of H₂ in *S2* suggests a more H₂-poor environment in *S2* than in OMC-1. It also seems to be difficult to reconcile the large blue-shift velocity with the outflow origin. The strong similarity of the *S2* spectra to those toward the ejecta knots in the Cas A SNR suggests that *S2* may be associated with SN ejecta. EGO G318.05+0.09 is located within the SNR G318.2+0.1, however, there is no supporting evidence for infrared emission associated with this SNR. There is no other evidence to relate *S2* with SN ejecta. Observations with high spectral resolution and better quality are definitely needed to draw a clear conclusion on the nature of *S2*.

The present observation suggests that the greenish color of EGOs has various origins and that one EGO could contain more than one objects of different types. It demonstrates significance of infrared spectroscopy for the study of the nature of individual objects. There might be similar CO emission associated in EGOs.

The authors thank the referee W. Reach for very useful comments, which greatly improved the paper. This work is based on observations with *AKARI*, a JAXA project with the participation of ESA. The authors thank all the members of the *AKARI* project for their continuous support. They would also like to thank Fumihiko Usui for his help in the data reduction, Bon-Chul Koo for the information on the SNR G318.2+0.1, and François Boulanger for useful discussion. This research has made use of the NASA/IPAC Infrared Science Archive, which is operated by the Jet Propulsion Laboratory, California Institute of Technology, under contract with the National Aeronautics and Space Administration. The laboratory data of the H₂O ice are obtained from the Leiden atomic and molecular database. TM received financial support from a Grant-in-Aid for JSPS Fellows. AA was supported by the University of Tokyo Research Internship Program (UTRIP) of 2014, which initiated this work. This work is supported by Grants-in-Aid for Scientific Research from the Japan Society for the Promotion of Science (nos. 23103004 and 16H00934).

Facilities: AKARI, Spitzer

REFERENCES

- Baba, S., Nakagawa, T., Shiharata, M., et al. 2016, *PASP*, 68, 27
 Barlow, M. J., Krause, O., Swinyard, B. M., et al. 2010, *A&A*, 518, 138

- Barlow, M. J., Swinyard, B. M., Owen, P. J., et al. 2013, *Sci*, 342, 1343
- Benjamin, R. A., Churchwell, E., Babler, B. L., et al. 2003, *PASP*, 115, 953
- Bianchi, S., & Schneider, R. 2007, *MNRAS*, 378, 973
- Biscaro, C., & Cherchneff, I. 2014, *A&A*, 564, A25
- Biscaro, C., & Cherchneff, I. 2016, *A&A*, 589, A132
- Bocchino, F., Parmar, A. N., Mereghetti, S., et al. 2001, *A&A*, 367, 629
- Caratti o Garatti, A., Stecklum, B., Linz, H., Garcia Lopez, R., & Sanna, A. 2015, *A&A*, 573, A82
- Casswell, J. 2009, *PASA*, 26, 454
- Clayton, D. D., Deneault, E. A.-N., & Meyer, B. S. 2001, *ApJ*, 562, 480
- Cyganowski, C. J., Whitney, B. A., Holden, E., et al. 2008, *ApJ*, 136, 2391
- Dwek, E., & Arendt, R. G. 2015, *ApJ*, 810, 75
- Ehrenfreund, P., Boogert, A. C. A., Gerakines, P. A., et al. 1996, *A&A*, 315, L341
- Gall, C., Hjorth, J., & Andersen, A. C. 2011, *A&A Rv*, 19, 43
- Gall, C., Hjorth, J., Watson, D., et al. 2014, *Nature*, 511, 326
- Geballe, T. R., & Garden, R. 1987, *ApJL*, 317, L107
- Geballe, T. R., & Garden, R. P. 1990, *ApJ*, 365, 602
- Gerakines, P. A., Schutte, W. A., Greenberg, J. M., & van Dishoeck, E. F. 1995, *A&A*, 296, 810
- Gerakines, P. A., Whittet, D. C. B., Ehrenfreund, P., et al. 1999, *ApJ*, 522, 357
- Gibb, E. L., Whittet, D. C. B., Boogert, A. C. A., & Tielens, A. G. G. M. 2004, *ApJS*, 151, 35
- Gomez, H. L., Krause, O., Barlow, M. J., et al. 2012, *ApJ*, 760, 96
- González-Alfonso, E., Wright, C. M., Cernicharo, J., Rosenthal, D., Boonman, A. M. S., & van Dishoeck, E. F. 2002, *A&A*, 386, 1074
- Green, J. A., Caswell, J. L., Fuller, G. A., et al. 2012, *MNRAS*, 420, 3108
- Indebetouw, R., Matsuura, M., Dwek, E., et al. 2014, *ApJL*, 782, L2
- Kamenetzky, J., McCray, R., Indebetouw, R., et al. 2013, *ApJL*, 773, L34
- Kotak, R., Meikle, P., Pozzo, M., et al. 2006, *ApJ*, 651, 118
- Lau, R. M., Herter, T. L., Morris, M. R., Li, Z., & Adams, J. D. 2015, *Science*, 348, 413
- Lee, H.-T., Liao, W.-T.; Froebrich, D., et al. 2013, *ApJS*, 208, 23
- Matsuura, M., Dwek, E., Meixner, M., et al. 2011, *Science*, 333, 1258
- Matsuura, M., Dwek, E., Barlow, M. J., et al. 2015, *ApJ*, 800, 50
- Mori, T. I., Onaka, T., Sakon, I., et al. 2014, *ApJ*, 784, 53
- Nath, B. B., Laskar, T., & Shull, J. M. 2008, *ApJ*, 682, 1055
- Neufeld, D. A., & Yuan, Y. 2008, *ApJ*, 678, 974
- Noble, J. A., Fraser, H. J., Aikawa, Y., Pontoppidan, K. M., & Sakon, I. 2013, *ApJ*, 775, 85
- Noriega-Crespo, A., Morris, P., Marleau, F. R., et al. 2004, *ApJS*, 154, 352
- Nozawa, T., Kozasa, T., Hbae, A., et al. 2007, *ApJ*, 666, 955
- Nozawa, T., Kozasa, T., Tominaga, N., et al. 2010, *ApJ*, 713, 356
- Nummelin, A., Whittet, D. C. B., Gibb, E. L., Gerakines, P. A., & Chiar, J. E. 2001, *ApJ*, 558, 185
- Ohyama, Y., Onaka, T., Matsuhara, H., et al. 2007, *PASJ*, 59, S411
- Onaka, T., Matsuhara, H., Wada, T., et al. 2007, *PASJ*, 59, S401
- Onaka, T., Lorente, R., Ita, Y., Ohyama, Y., Tanabé, T., & Pearson, C. 2009, *AKARI IRC Data User Manual for Post-Helium (Phase 3) Mission*, ver1.1, http://www.ir.isas.jaxa.jp/AKARI/Observation/support/IRC/IDUM/IRC_IDUM_P3_1.1.pdf
- Onaka, T., Matsuhara, H., Wada, T., et al. 2010, *Proc. SPIE*, 7731, 77310M
- Pontoppidan, K. M., Boogert, A. C. A., Fraser, H. J., et al. 2008, *ApJ*, 678, 1005
- Qiu, K., Zhang, Q., Megeath, S. T., et al. 2008, *ApJ*, 685, 1005
- Reach, W. T., Rho, J., Tappe, A., et al. 2006, *AJ*, 131, 1479
- Rho, J., Onaka, T., Cami, J., & Reach, W. T., et al. 2012, *ApJL*, 747, L6
- Richter, M. J., Graham, J. R., & Wright, G. S. 1995, *ApJ*, 454, 277
- Rosenthal, D., Bertoldi, F., & Drapatz, S. 2000, *A&A*, 356, 705
- Shimonishi, T., Onaka, T., Kato, D., et al. 2010, *A&A*, 514, A12
- Sibthorpe, B., Ade, P. A. R., Bock, J. J., et al. 2010, *ApJ*, 719, 1553
- Silvia, D. W., Smith, B. D., & Shull, J. M. 2010, *ApJ*, 715, 1575
- Silvia, D. W., Smith, B. D., & Shull, J. M. 2012, *ApJ*, 748, 12
- Smith, R. G., Sellgren, K., & Brook, T. Y. 1993, *MNRAS*, 263, 749
- Smith, H. A., Hora, J. L., Marengo, M., & Pipher, J. L. 2006, *ApJ*, 546, 1264
- Takami, M., Karr, J. L., Koh, H., Chen, H.-H., & Lee, H.-T. 2010, *ApJ*, 720, 155
- Takami, M., Chen, H.-H., Karr, J. L., et al. 2012, *ApJ*, 748, 8
- Temim, T., & Dwek, E. 2013, *ApJ*, 774, 8
- Thi, W.-F., van Dishoeck, E. F., Dartois, E., et al. 2006, *A&A*, 449, 251
- Tobin, J. J., Harman, L., Calvet, N., & D'Alessio, P. 2008, *ApJ*, 679, 1364
- Tinyanont, S., Kasliwal, M. M., Fox, O. D., et al. 2016, *ApJ*, submitted (arXiv:1601.03440)
- Wallström, S. H., Biscaro, C., Salgado, F., et al. 2013, *A&A*, 558, L2
- Walsh, A. J., Hyland, A. R., Robinson, G., & Burton, M. G. 1997, *MNRAS*, 291, 261
- Wesson, R., Barlow, M. J., Matsuura, M., & Ercolano, B. 2015, *MNRAS*, 446, 2089
- Whiteoak, J. B. Z., & Green, A. J. 1996, *A&AS*, 118, 329